Creation of new guest accessible space under gas pressure in a flexible MOF: Multidimensional insight through combination of in situ techniques

Prashant M. Bhatt, Eustina Batisai, Vincent J. Smith and Leonard J. Barbour*

Supporting information

Materials: All materials were purchased from Sigma Aldrich and used without further processing or purification.

Single crystal diffraction: SCD intensity data were collected using a Bruker APEX II DUO diffractometer using graphite monochromated Mo Kα radiation (λ = 0.7107 Å). Where indicated, crystals were subjected to controlled pressures using an environmental gas cell. Temperature control was maintained using an Oxford Cryosystems Cryostat (700 Series Cryostream Plus) for data collection of **3** at 253 K. Data were collected using omega scans and recorded using a CCD (charge coupled device) area detector. Data reduction and absorption corrections were carried out using the programs SAINT[1] and SADABS,[2] which form part of the APEX II software package. Space groups were assigned based on systematic absences and intensity statistics using the program XPREP. The structures were solved by direct methods using SHELXS-97 [3] and expanded/refined using SHELXL-97[3] within the X-Seed[4] graphical user interface. Unless otherwise stated, non-hydrogen atoms were refined anisotropically by means of full-matrix least squares calculations on F^2. In all cases, hydrogen atoms were placed in calculated positions using riding models.

CCDC deposition numbers:
CCDC 1429431: Crystal 1_ form **1**$_{CO2}$
CCDC 1429432: Crystal 1_ form **2**
CCDC 1429433: Crystal 1_ form **3** (10bar, -20C)
CCDC 1429434: Crystal 2_ form **2**
CCDC 1429435: Crystal 2_ form **3** (20 bar, RT)

Powder X-ray diffraction: PXRD studies were carried out using a PANalytical X'Pert PRO instrument. A sample of **2** was gently ground before being transferred into 0.3 mm glass capillary of the environmental gas cell for variable pressure measurements. Before each measurement the sample was allowed to equilibrate at the desired pressure for at least 8 hours. Data were collected in the 2θ range 5-40°.

Pressure-ramped DSC measurements: High pressure DSC measurements were carried out using a Setaram μDSC7 Evo module equipped with a high pressure sample holder. For pressure gradient measurements the DSC instrument was coupled to a Teledyne ISCO 260D syringe pump. The syringe pump was controlled by a computer running software that was developed in-house. The software regulates the motion of the syringe plunger such that a constant pressure-time gradient is maintained. Data were recorded and analysed using the Calisto software package from Setaram.

A 32.2 mg sample of **2** (i.e. the activated form of **1**) was crushed and placed in the DSC sample chamber. The heat flow was recorded while increasing the CO_2 pressure at a rate of 0.2 bar min^{-1} in the range 2 to 25 bar. The temperature of the sample and reference chambers was maintained at 25 °C. Thereafter the pressure was decreased at the same rate.

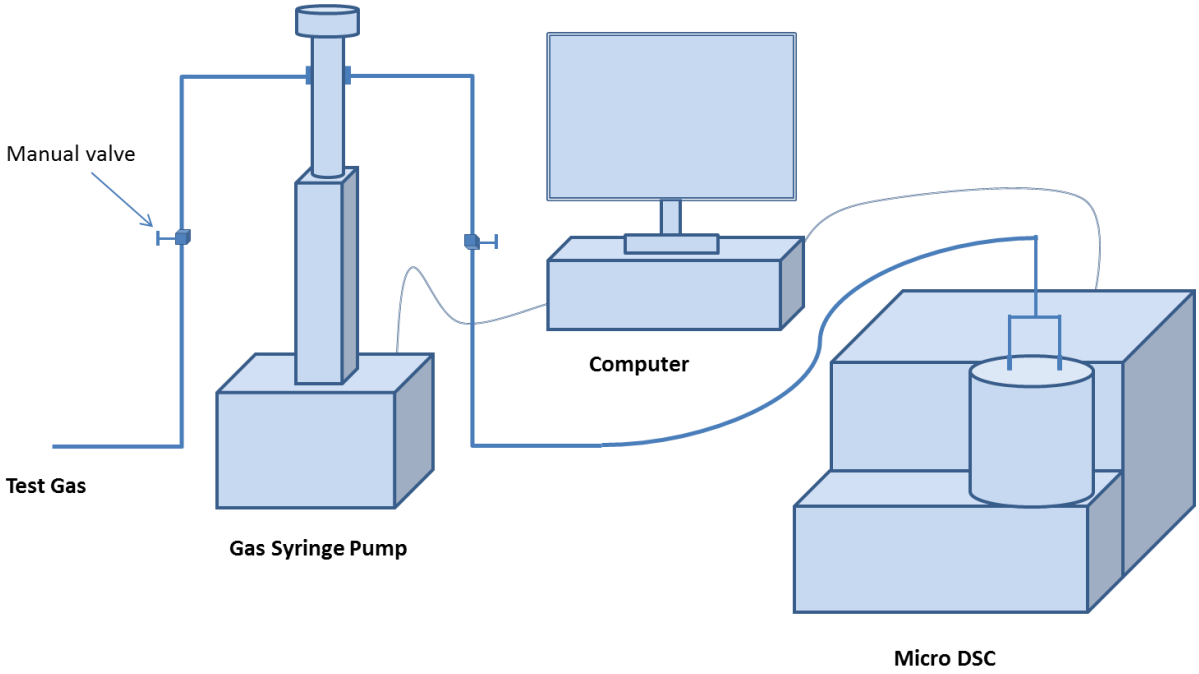

Sorption measurements: Sorption measurements were carried out using a Hy-Energy PCTPro-2000 equipped with a Microdoser module. Data were recorded in the pressure range 0-30 bar at intervals of approximately 1 bar of the test gas.

Table S1. Crystallographic data for structure **1**$_{CO2}$, **2** and **3**

	2	**1**$_{CO2}$	**3** at 10bar, -20 °C	**3** at 20 bar, RT
Empirical formula	$C_{13}H_8NO_4Zn$	$C_{26}H_{16}N_2O_8Zn_2$	$C_{26.86}H_{16}N_2O_{9.73}Zn_2$	$C_{26}H_{16}N_2O_8Zn_2$
Formula weight	307.57	615.15	653.22	615.15
Temperature (K)	298(2)	298(2)	253(2)	298(2)
Wavelength (Å)	0.71073	0.71073	0.71073	0.71073
Crystal system	Triclinic	Triclinic	Monoclinic	Monoclinic
a/Å	7.9917(13)	10.887(5)	14.099(10)	14.065(8)
b/ Å	9.4227(16)	10.896(4)	10.997(8)	10.949(6)
c/ Å	10.5835(17)	14.070(6)	21.865(15)	21.771(13)
α°	65.314(2)	91.252(4)	90	90
β°	86.464(2)	92.588(5)	93.971(9)	94.319(9)
γ°	76.513(2)	104.430(5)	90	90
Space group	*P*-1	*P*-1	$P2_1/c$	$P2_1/c$
Volume (Å^3)	703.6(2)	1613.9(11)	3382(4)	3343(3)
Z	2	2	4	4
Calculated density (g cm^{-3})	1.452	1.266	1.283	1.222
Absorption coefficient (mm^{-1}	1.752	1.528	1.466	1.475
F_{000}	310	620	1316	1240
Crystal size (mm^3)	0.16 x 0.14 x 0.07	0.16 x 0.14 x 0.07	0.16 x 0.14 x 0.07	0.19 x 0.14 x 0.07
Range for data collection (θ°)	2.12 to 26.05	1.45 to 26.4	1.87 to 26.21	1.88 to 26.05
Miller index ranges	$-9 \le h \ge 9$, $-11 \le k \ge 7$, $-13 \le l \ge 12$	$-13 \le h \ge 13$, $-13 \le k \ge 13$, $-17 \le l \ge 17$	$-16 \le h \ge 16$, $-13 \le k \ge 13$, $-21 \le l \ge 26$	$-17 \le h \ge 17$, $-13 \le k \ge 13$, $-26 \le l \ge 26$
Reflections collected	4201	16692	17291	36943
Independent reflections	2657 [R_{int} = 0.0204]	6440 [R_{int} = 0.0881]	6579 [R_{int} = 0.0827]	6587 [R_{int} = 0.0942]
Completeness to θ_{max} (%)	95.8	97.2	96.5	99.6
Max. and min. transmission	0.8872 and 0.7669	0.9006 and 0.7921	0.9004 and 0.799	0.904and 0.768
Refinement method	Full-matrix least-squares on F^2	Full-matrix least-squares on F^2	Full-matrix least-squares on F^2	Full-matrix least-squares on F^2
Data / restraints / parameters	2657 / 0 / 164	6440 / 0 / 323	6579 / 0 / 328	6587 / 0 / 327
Goodness-of-fit on F^2	1.251	1.023	1.081	0.988
Final *R* indices [$I>2\sigma(I)$]	*R*1 = 0.0586, *wR*2 = 0.1744	*R*1 = 0.0862, *wR*2 = 0.2061	*R*1 = 0.0877, *wR*2 = 0.2116	*R*1 = 0.0633, *wR*2 = 0.1578
R indices (all data)	*R*1 = 0.0730, *wR*2 = 0.2199	*R*1 = 0.1384, *wR*2 = 0.2228	*R*1 = 0.1408, *wR*2 = 0.2319	*R*1 = 0.0955, *wR*2 = 0.1718
Largest diff. peak and hole (e Å^{-3})	1.265 and -1.253	1.772and -1.120	2.296 and -0.731	1.532 and -1.022

Structural comparison of $\mathbf{1}_{CO2}$ and 3

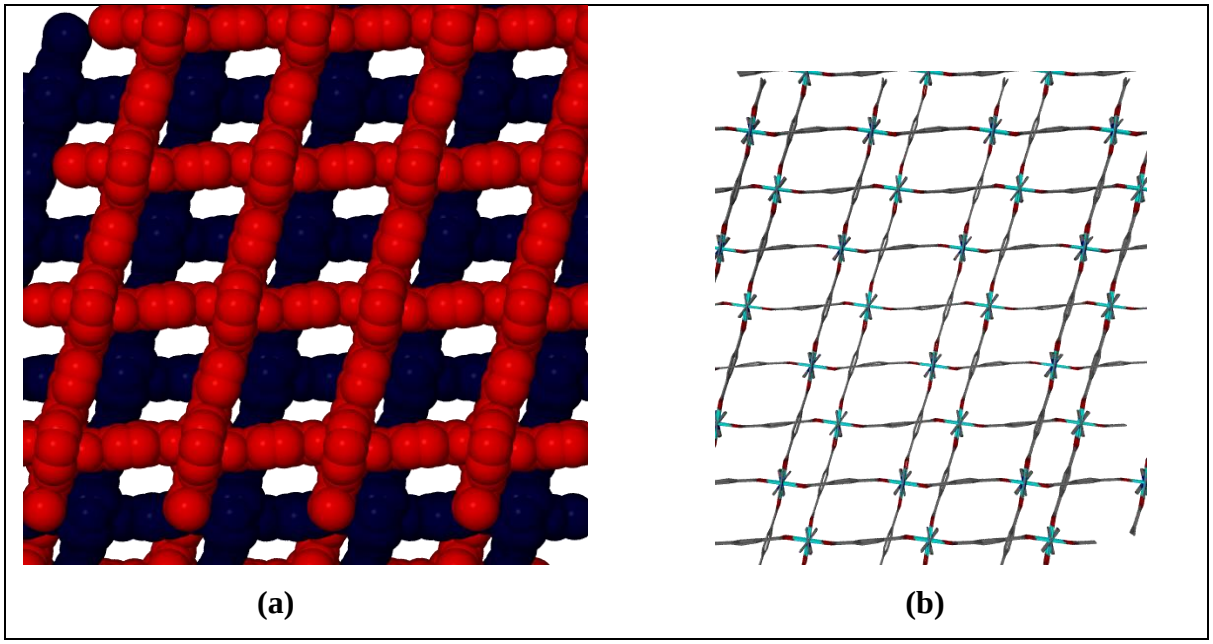

Figure S1. View along the *c* axis of $\mathbf{1}_{CO2}$ (RT)

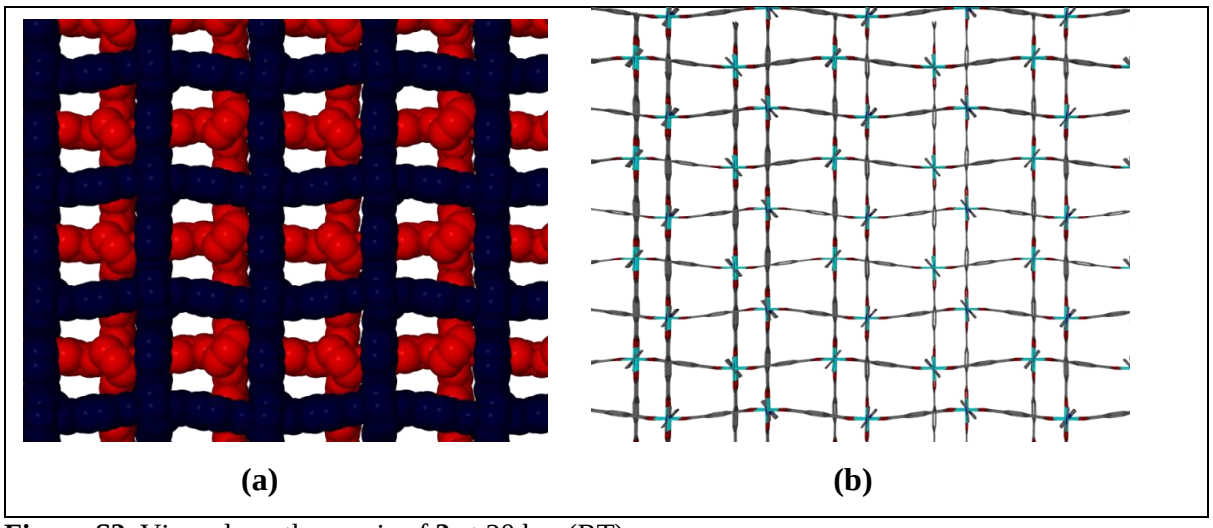

Figure S2. View along the *a* axis of **3** at 20 bar (RT)

Structures $\mathbf{1}_{CO2}$ and **3** are both based on the zinc paddlewheel SBU with the same overall connectivity. A number of changes, most of them relatively small, occur during the structural transformation from $\mathbf{1}_{CO2}$ to **3**, including a change in the relative positions of the

linkers and their coordination geometries, relative movement of the two interpenetrating networks and a change in the molecular geometry of some of the linkers.

The major structural difference between **1**$_{CO2}$ to **3** involves a change in the shape of the grid formed by dinuclear zinc paddle-wheel SBU and the bdc linkers. In the structure of **1**$_{CO2}$, the grid is slightly tilted and resembles a rhombus in shape, while in the structure of **3** the linkers are comparatively orthogonal and the grid units resemble a square (Figs. S1 and S2).

Another difference between **1**$_{CO2}$ and **3** involves the torsion angles of the carboxylate groups of the bdc linkers as given in Table S2. A more profound change is observed in the bdc linkers of **1**$_{CO2}$ and $_3$ as viewed along the *a* axis, where the torsion angles change from 8.4(8)^o and 3.8(6)^o to 9.5(3)^o and 8.0(3)^o respectively. Although the changes in the torsion angle is not very large by itself, in combination with change in square grid and other subtle structural change ultimately create space for extra CO_2 molecule.

Table S2. Torsion angles between carboxylate groups and phenyl ring of bdc linkers in **1**$_{CO2}$ and **3**

Torsion angles for 1$_{CO2}$		**Torsion angles for 3**	
BDC1	BDC2	BDC1	BDC2
8.4(8)^o	4.9(8)^o	9.5(3)^o	5.3(2)^o
3.8(6)^o	3.2(9)^o	8.0(3)^o	2.3(1)^o

Structural differences between **1**$_{CO2}$, **2** and **3** are highlighted by overlaying of respective structures in Figures S3-S5.

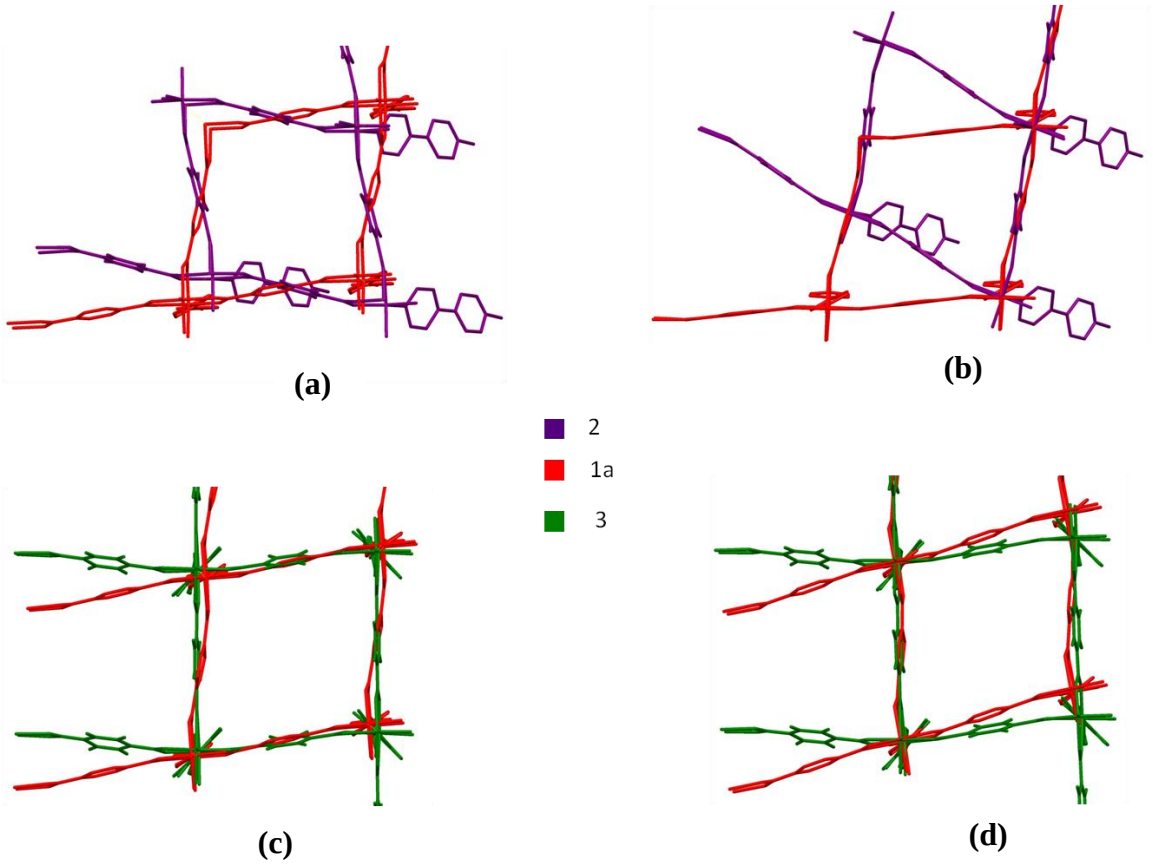

Figure S3. Structure overlays of **2** and **1**$_{CO2}$ (a) overlaying all four Zn_2 units and (b) overlaying only two Zn_2 units. Structure overlays of **3** and **1**$_{CO2}$ (c) overlaying all four Zn_2 units and (d) overlaying only two Zn_2 units.

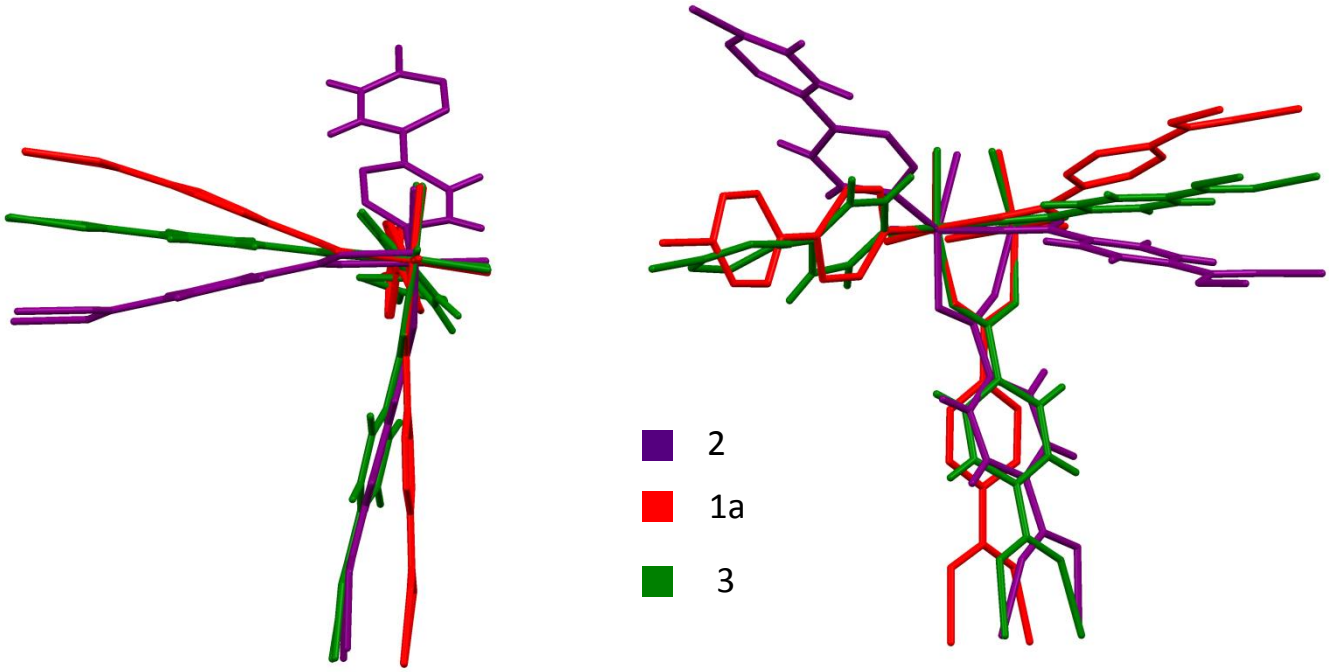

Figure S4. Structure overlay of **2, 1**$_{CO2}$ and **3** from different views.

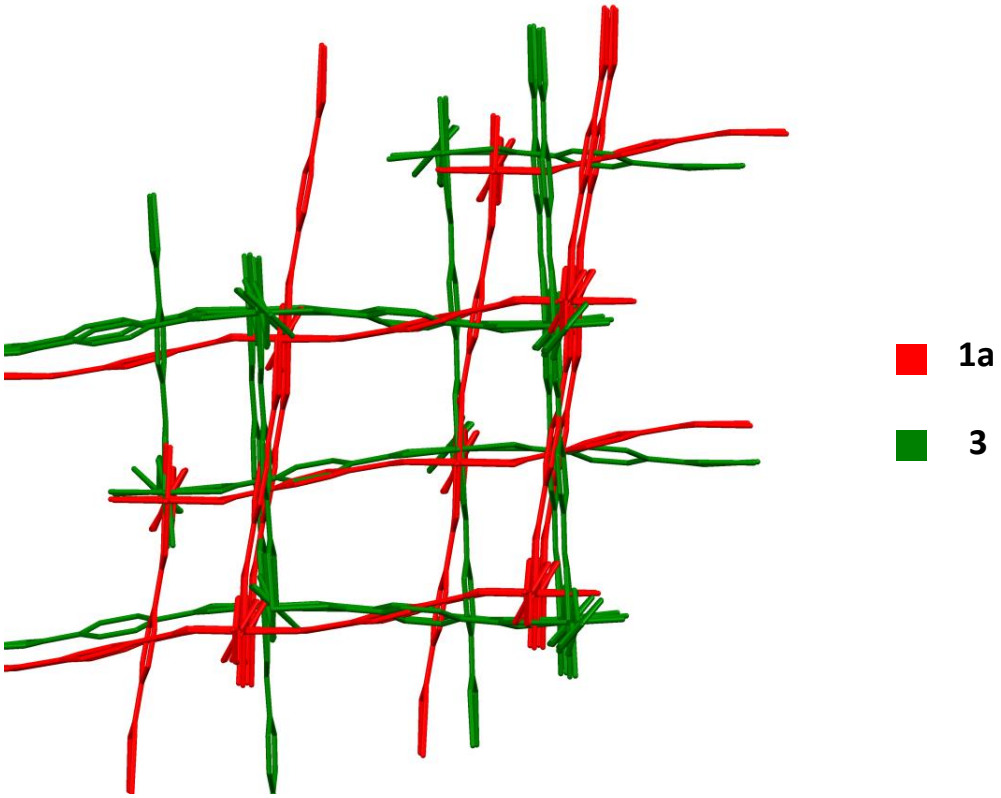

Figure S5. Structure overlay of interpenetrating networks of **1**$_{CO2}$ and **3**.

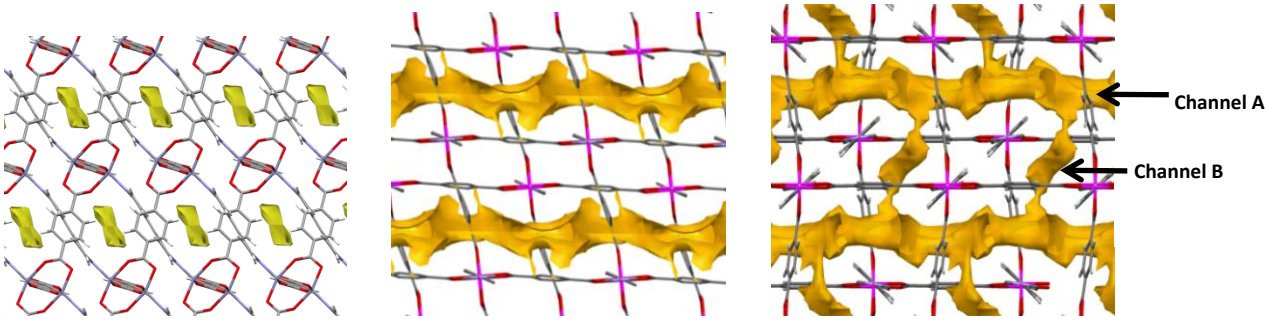

(a) **(b)** **(c)**

Figure S6. (a) Solvent-accessible space in **2** (elongated 0D voids). (b) solvent accessible space in **1**$_{CO2}$; note that channels are only interconnected in two dimensions parallel to the *bc* plane. (c) solvent accessible space in **3** - the two dimensional channel networks observed for **1**$_{CO2}$ are connected to each other by newly formed channels.

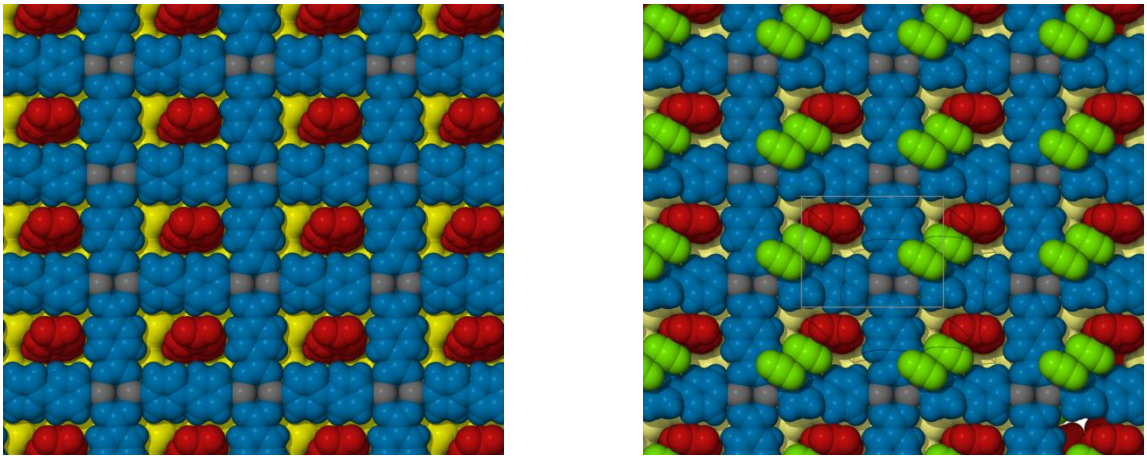

(a) **(b)**

Figure S7. Space-filling model of (a) $\mathbf{1}_{CO2}$ and (b) **3**, illustrating the structural changes that result in the formation of new guest-accessible space that becomes occupied by two CO_2 molecules during the transition from $\mathbf{1}_{CO2}$ to **3**

Comment on determining void volumes using crystal structure data.

It is worth noting that calculated void volumes should be treated with considerable caution. The calculations can be susceptible to a number of factors that markedly affect the outcome and some of these are briefly discussed below. The choice of probe radius needs to be considered carefully – for example, a probe the size of a hydrogen atom is not a suitable choice for assessing the volume available to a CO_2 molecule. Different computer programs often use different van der Waals radii for atoms and the radii assigned to the atoms that line the void will therefore affect the outcome of similar calculations by the different programs. If parts of the structure are statically disordered then it is difficult to assess which of the many different combinations of fragment orientations should be used. Dynamic disorder presents an even more difficult challenge. Moreover, all of the programs currently available for void volume calculations assume that atomic coordinates are frozen in space and do not take the abovementioned factors or even normal thermal motion into account. Therefore, in reality, void spaces may differ from one region of the structure to another at any instant in time and void shapes may experience considerable dynamic distortion. While determination of void volumes, especially in dynamic structures, are of some qualitative value for assessing potential porosity it should be remembered that these values are not absolute and that the calculations do not meet the criteria for acceptable scientific rigour.

PG-DSC experiments to study other gas pressure induced phase transformations reported in literature

The PG-DSC technique was further used to detect gas pressure induced gate-opening phase transformations in materials known from the literature. PG-DSC experiments for these materials are discussed below.

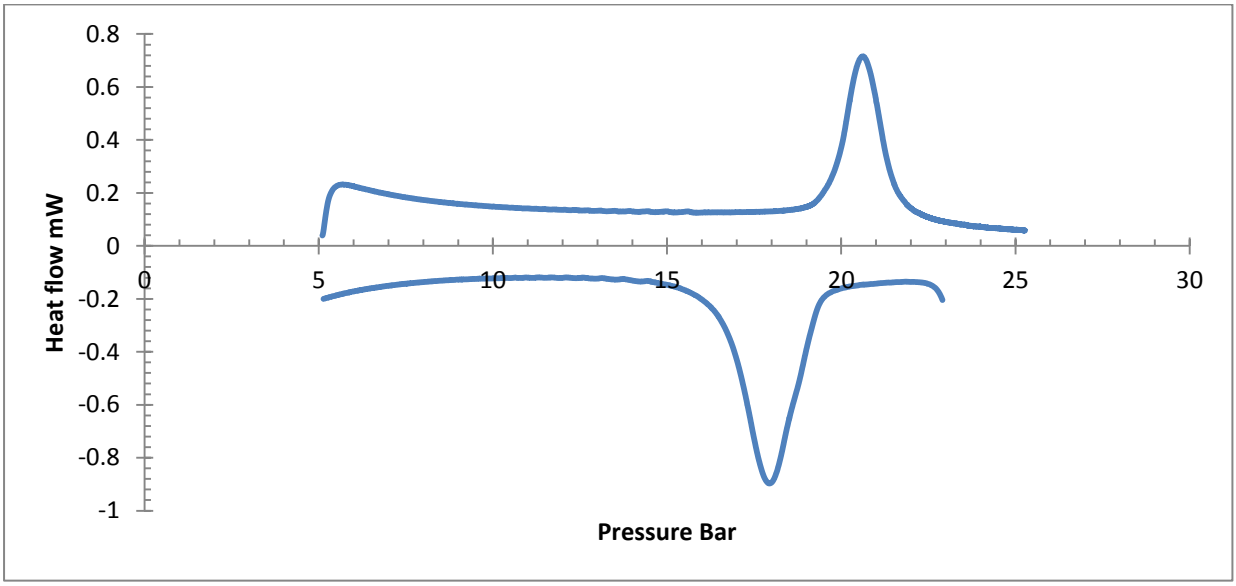

Figure S8. PG-DSC of the system $[Cu_2(benzoate)_4(pyz)]$.[5] The guest-free structure of the system contains empty cages and, under CO_2 gas pressure the materials undergoes a phase transition to a new structure with 1-D channels that include CO_2 molecules. Gate-opening under CO_2 pressure can be monitored by PG-DSC as an exotherm between 20-23 bar pressure of CO_2 and the gate-closing transition as an endotherm between 20-15 bar pressure of CO_2.

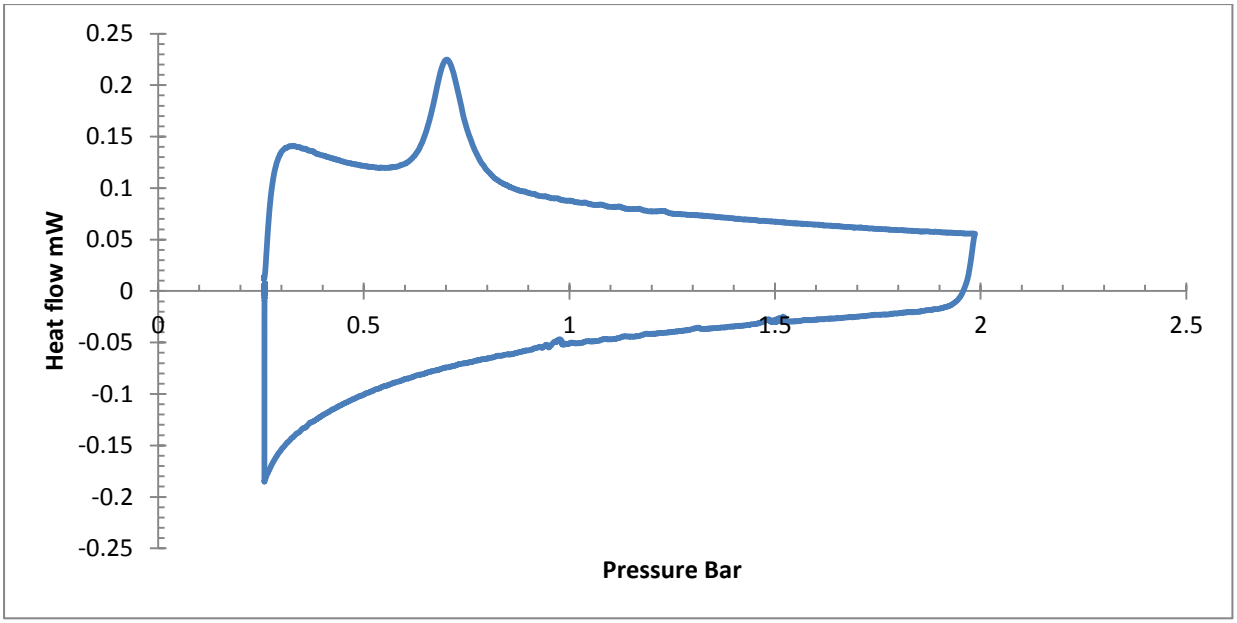

Figure S9. PG-DSC of the system $[Cu(BF_4)_2(bpy)_2]$. The system undergoes gas pressure induced phase transition under CO_2 pressure.[6] The distance between two neighboring quasi-square grids increases under CO_2 pressure due to formation of a CO_2 clathrate. The exotherm between 0.6-0.8 bar of CO_2 pressure in PG-DSC trace indicates pressure induced gate-opening and the reverse conversion occurs below the starting pressure of 0.25 bar CO_2 pressure (and hence the corresponding endotherm could not be observed).

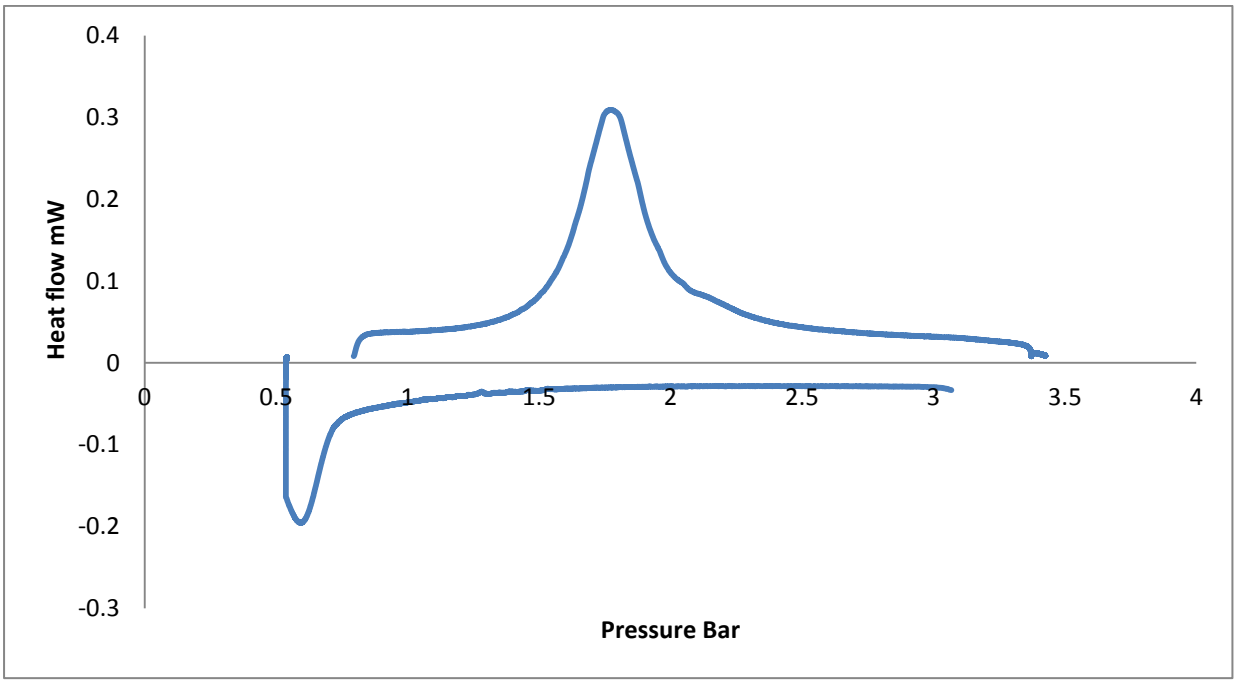

Figure S10. PG-DSC of the system $[Cu_2(bdc)_2(bpy)]$, a Cu analogue of the system $[Zn_2(bdc)_2(bpy)]$. The closed guest-free form of $[Cu_2(bdc)_2(bpy)]$ opens up under gas pressure to form a guest-included open form.[7] The exotherm between 1.5 bar and 2.5 bar of CO_2 at 25 °C in PG-DSC indicates

transformation from the closed to the open structure. It is interesting to note that how similar structures based on different metal ions can have considerably different gate-opening pressures.

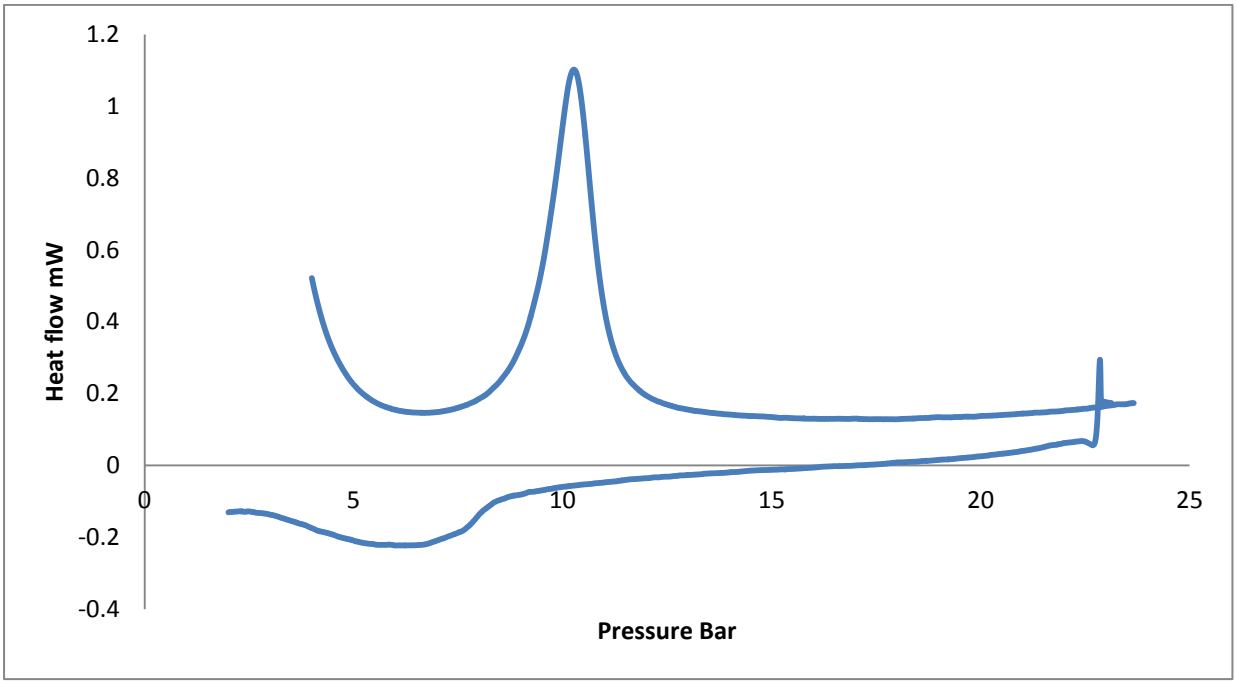

Figure S11. PG-DSC trace showing the gas-induced transformation of the guest-free dense phase of *p-tert*-butylcalix[4]arene to the low density phase.[8] The exotherm around 10 bar CO_2 pressure (at 0 °C) in the PG-DSC trace indicates the gate-opening phase transformation.

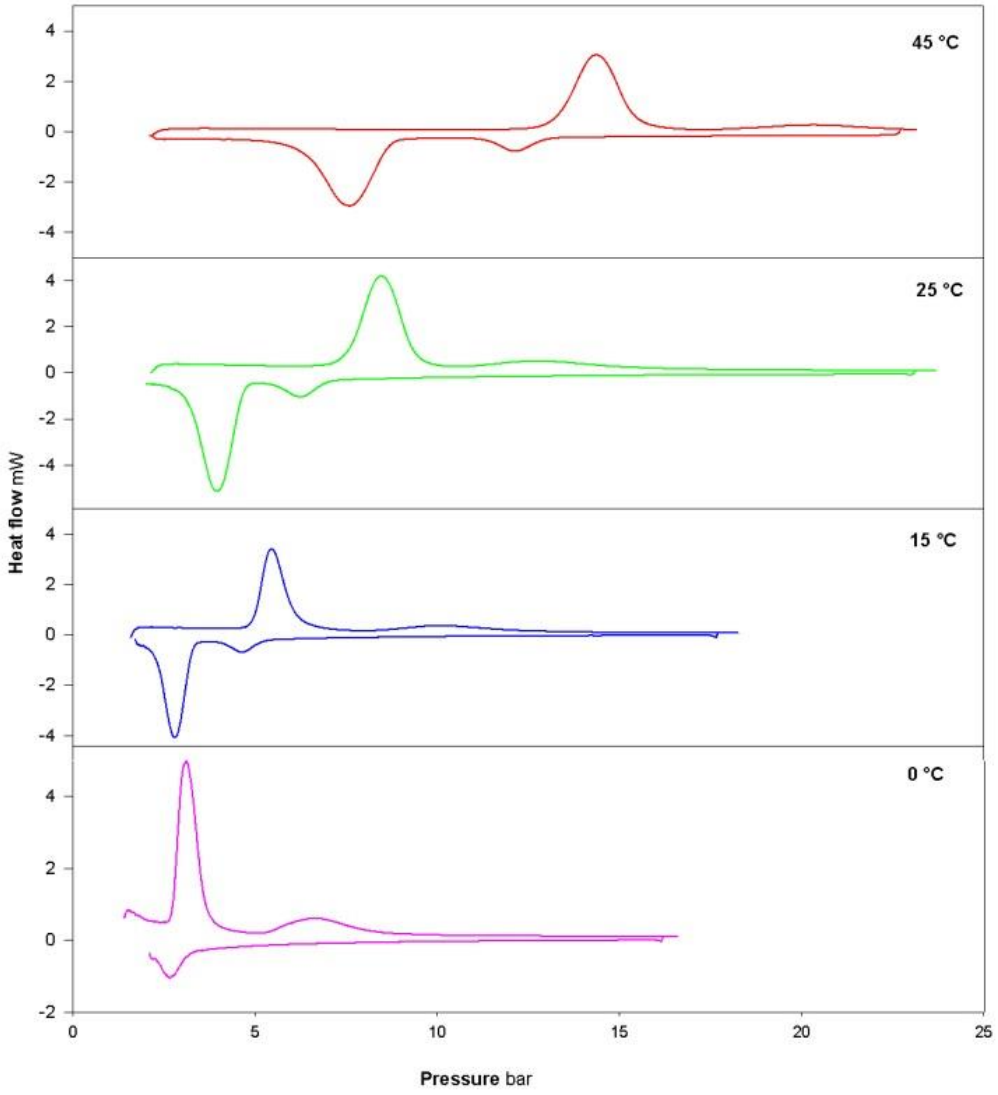

Figure S12. PG-DSC traces recorded at 0, 15, 25 and 45 °C for CO_2 sorption/desorption by $[Zn_2(bdc)_2(bpy)]$. Note the change in gate opening pressures and hysteresis with the temperature

PG-DSC of 2 under CH_4 at a constant pressure gradient

PG-DSC experiments were also carried out on **2** using CH_4 as the test gas at 0 ºC and 25 ºC, as shown in Figs. S12 and S13, respectively. The gate-opening pressure for CH_4 (ca 75 bar at 25 °C and ca 40 bar at 0 °C) is much higher than that for CO_2. Also, only one very broad peak is observed in the PDSC trace, indicating that the conversion is much slower with CH_4 than with CO_2

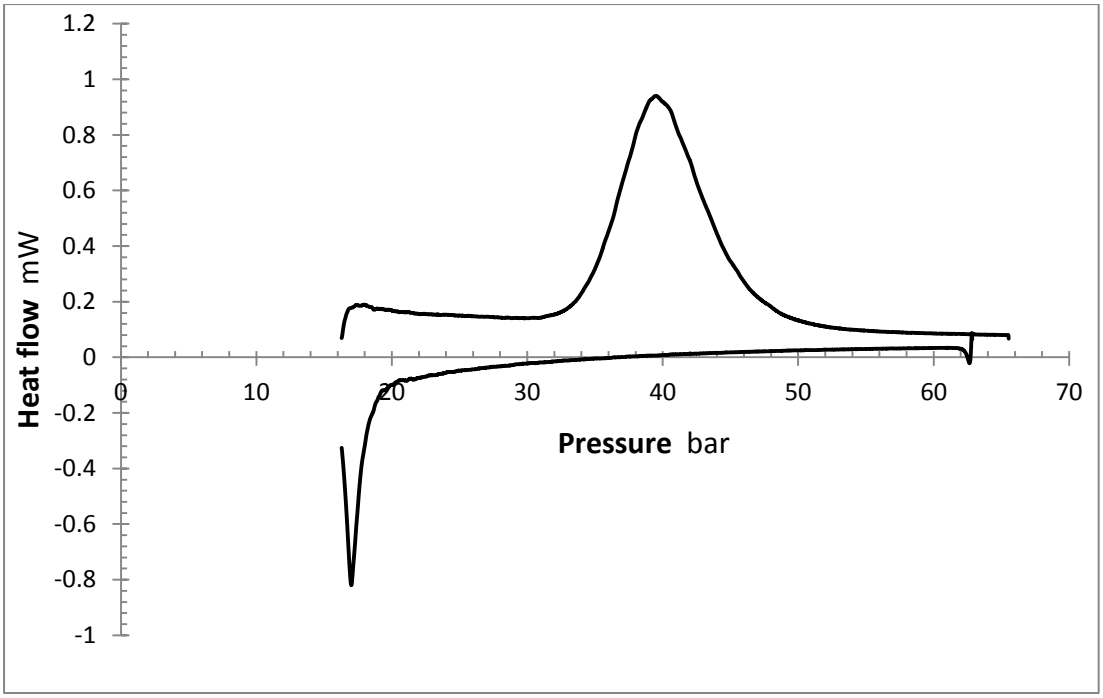

Figure S13. PDSC for **2** at 0 °C with a constant pressure gradient of 1 bar min^{-1} in the pressure range 16 to 65 bar of CH_4.

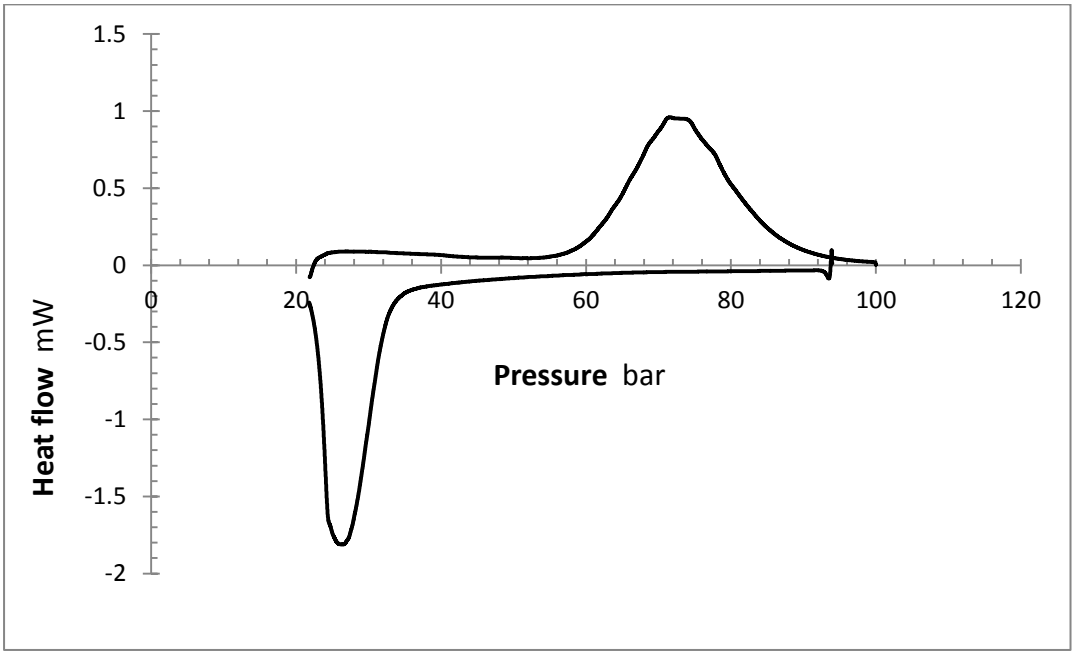

Figure 14. PDSC for **2** at 25 °C with a constant pressure gradient of 1 bar min^{-1} in the pressure range of 21 to 99 bar of CH_4.

Variable pressure PXRD experiments

The structural transformations of **2** into $\mathbf{1}_{CO2}$ and $\mathbf{1}_{CO2}$ into **3** (and vice versa) were also monitored at various pressures of CO_2 at 25 °C using PXRD (Figs. S15, S16). The information obtained from the PXRD traces is in agreement with data obtained from SCD, sorption experiments and PDSC experiments (Figs S17-S19). PXRD traces of **2** at various pressures of CH_4 at 25 °C indicate a phase change to a structure similar to **3** around 80 bar pressure of CH_4 as shown in the Figures S20 and S21.

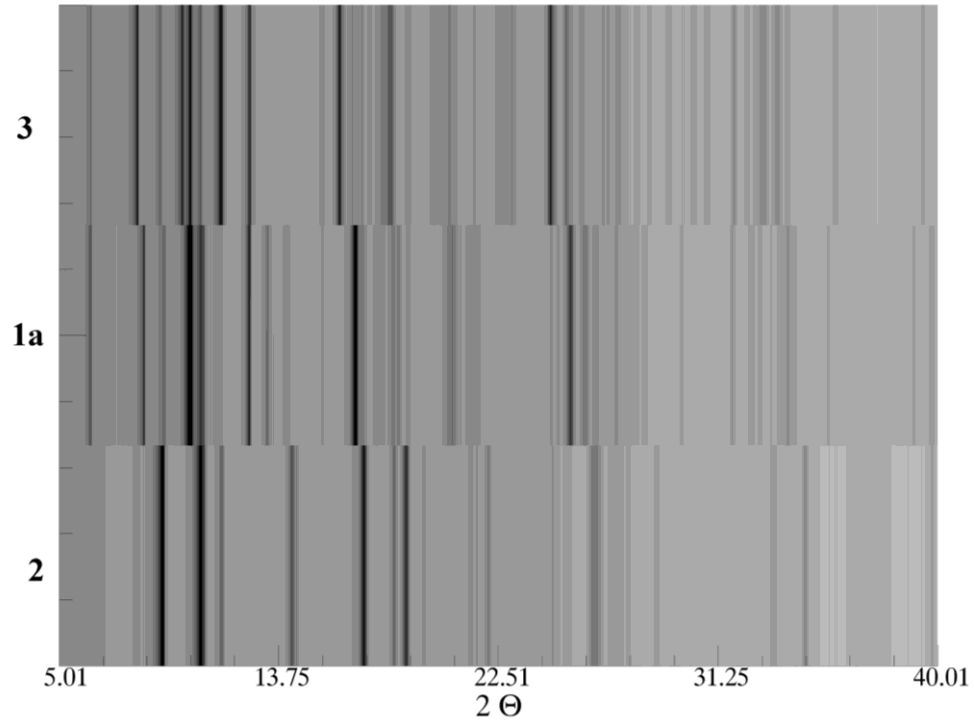

Figure S15. Comparison of PXRD patterns of **2**, $\mathbf{1}_{CO2}$ and **3** by recording PXRD patterns at 0 bar, 10 bar and 20 bar, respectively.

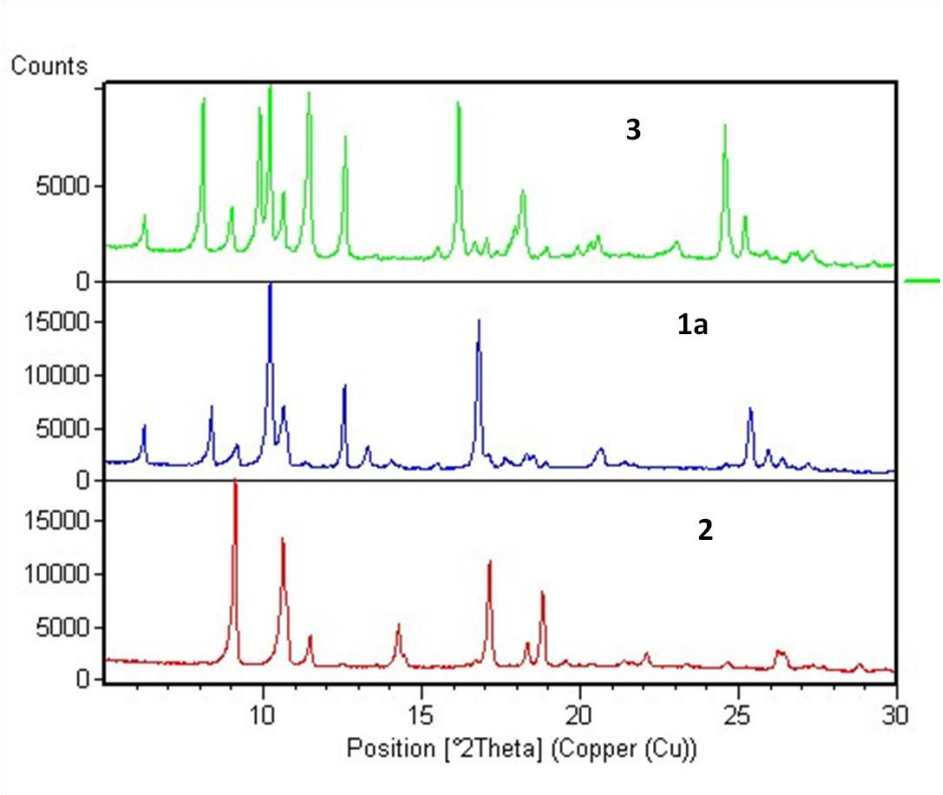

Figure S16. Comparison of PXRD patterns of **2**, **1**$_{CO2}$ and **3** by recording PXRD patterns at 0 bar, 10 bar and 20 bar respectively.

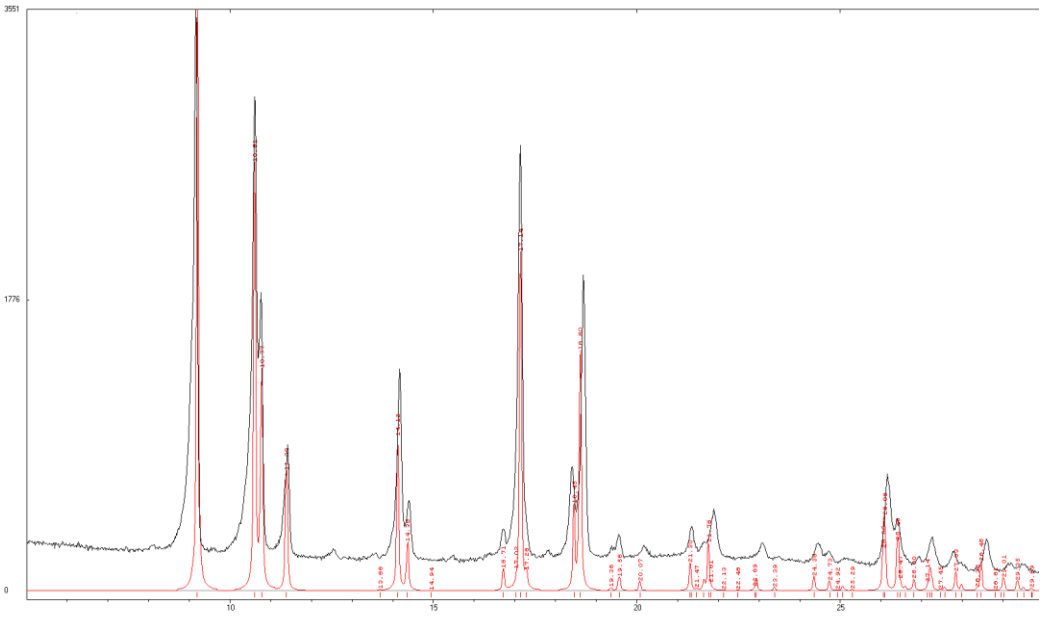

Figure S17. Comparison of simulated PXRD from SCD of **2** (red) and experimental PXRD of the sample at 0 bar CO_2 pressure (black).

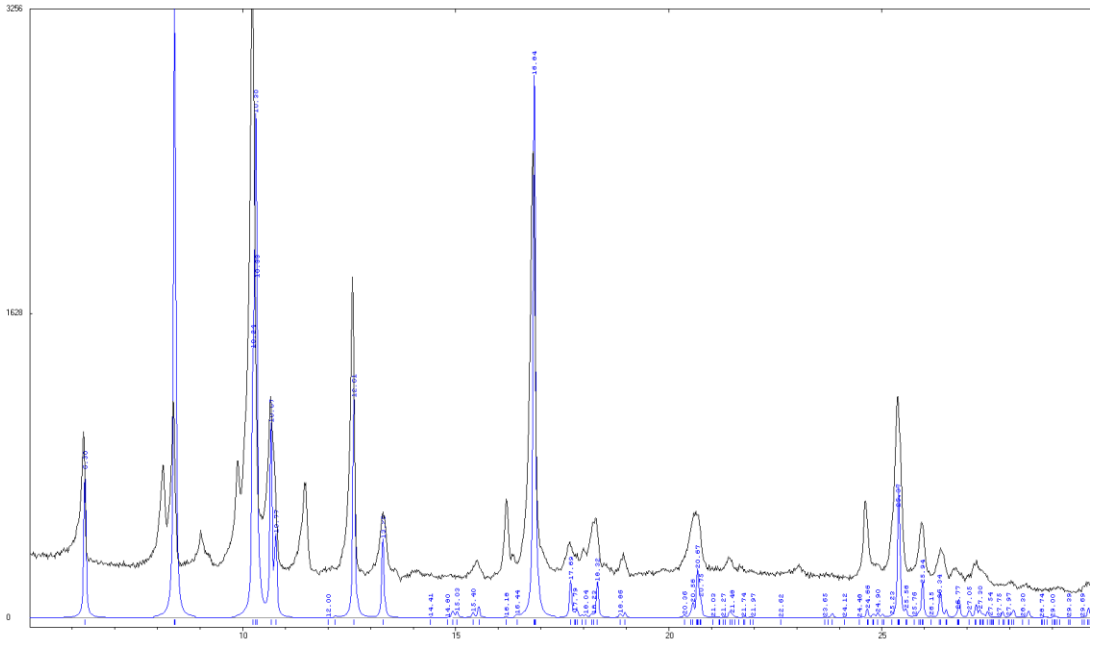

Figure S18. Comparison of simulated PXRD from SCD of **1**$_{CO2}$ (blue) and experimental PXRD of the sample at 10 bar CO_2 pressure (black). Note that under these conditions a small amount of form **3** coexists with form **1**$_{CO2}$ and is responsible for additional peaks in the experimental PXRD pattern.

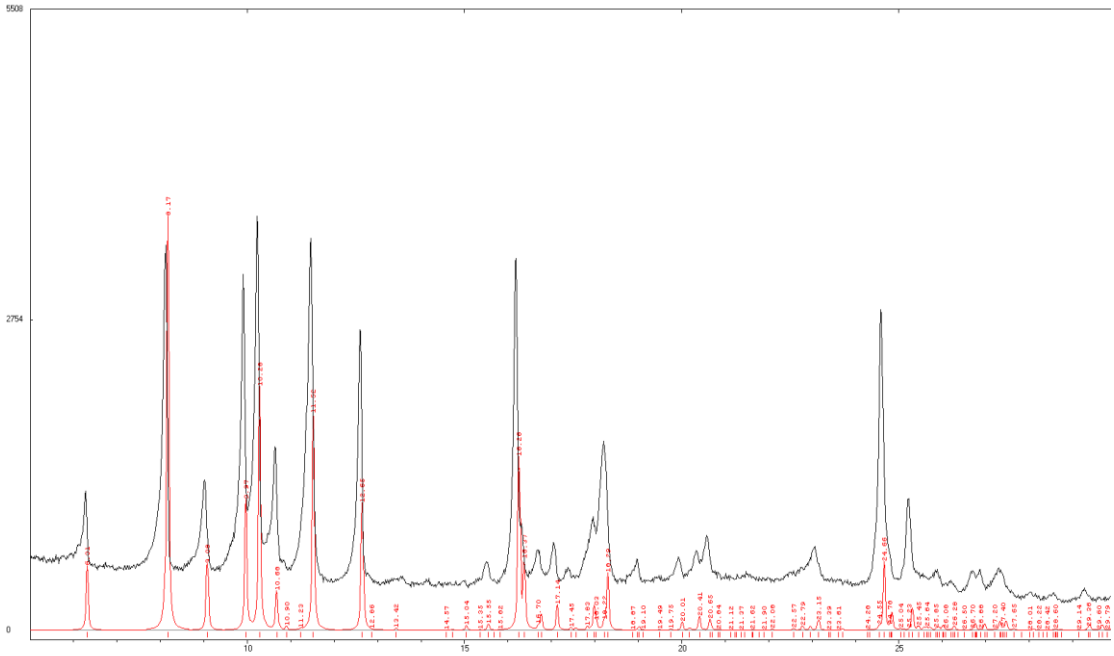

Figure S19. Comparison of simulated PXRD from SCD of **3** (red) and experimental PXRD of the sample at 20 bar CO_2 pressure (black).

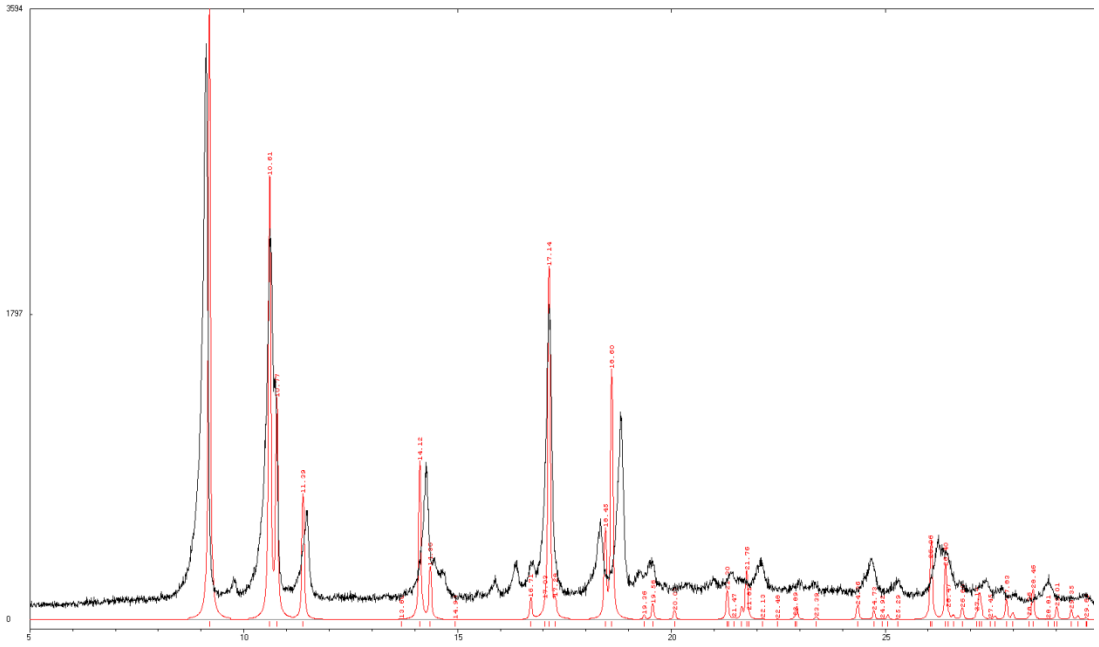

Figure S20. Comparison of simulated PXRD from SCD of **2** (red) and experimental PXRD of the sample at 0 bar (black).

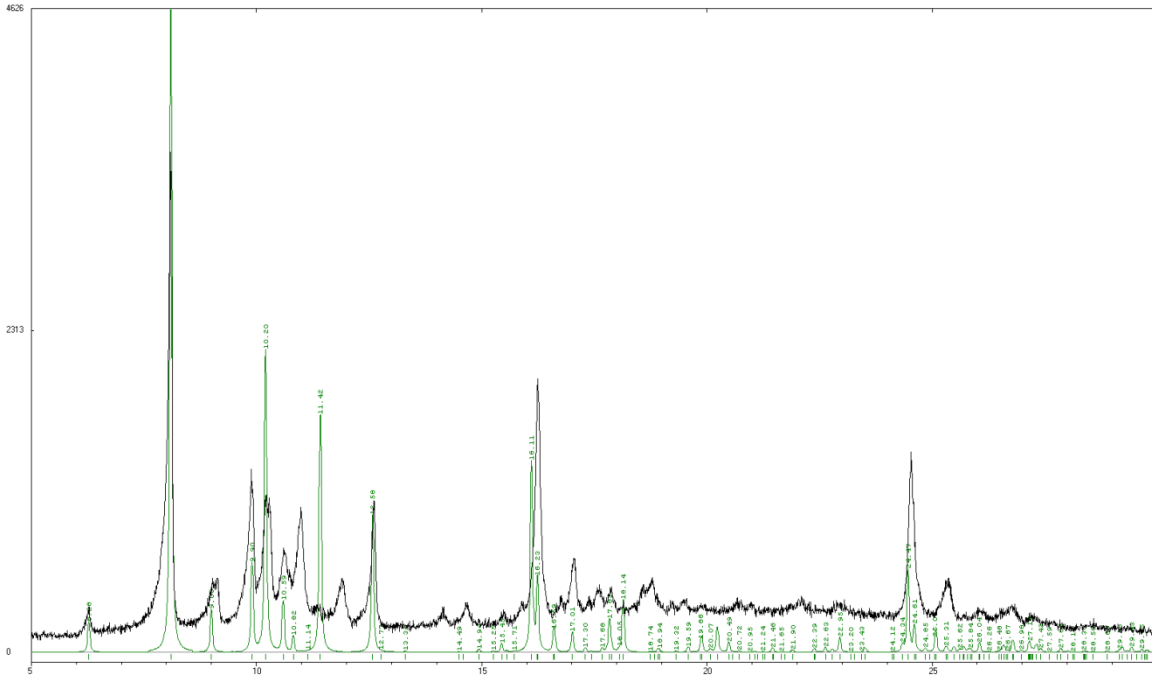

Figure S21. Comparison of simulated PXRD from SCD of **3** (green) and experimental PXRD of the sample at 80 bar CH_4 pressure (black).

Variable temperature CO_2 sorption experiments

Sorption experiments for CO_2 were carried out at different temperatures (0, 15, 25 and 45 °C) as shown in Figure S22. The isotherms correlate well with the data obtained from PG-DSC experiments at variable temperature.

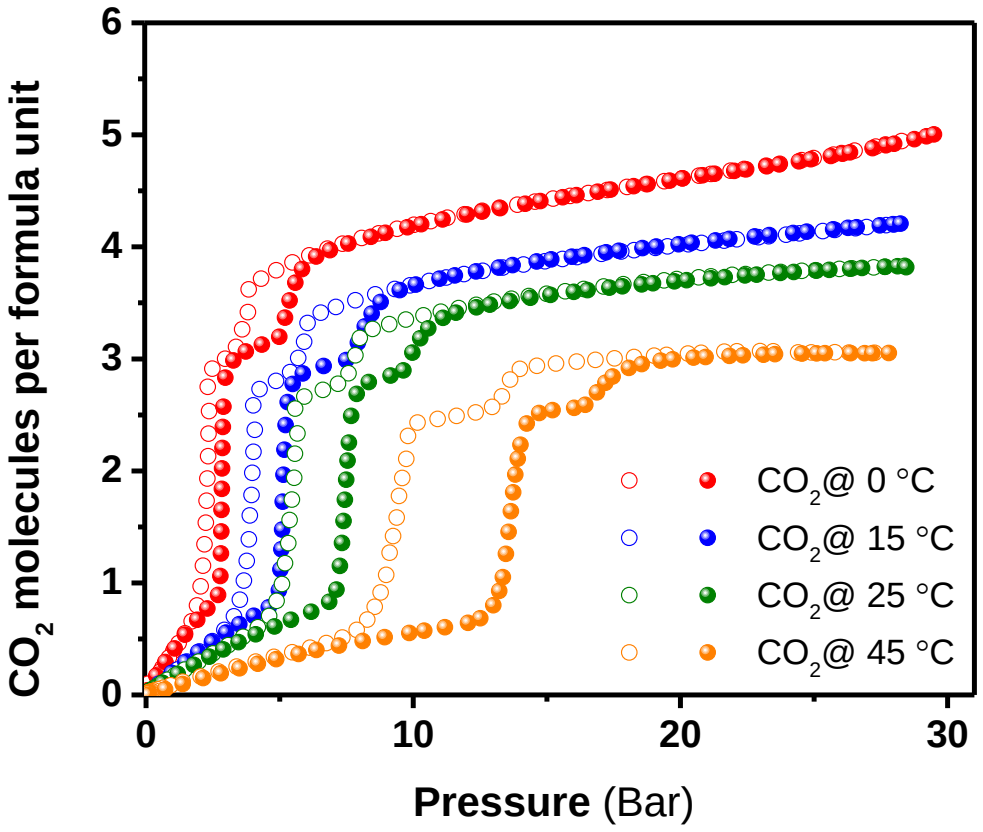

Figure S22. CO_2 isotherms for **2** recorded at different temperatures. Closed and open symbols represent sorption and desorption, respectively. The gate-opening pressure and hysteresis increase with increase in temperature.

[1] SAINT Data Reduction Software, Version 6.45, Bruker AXS Inc.; Madison, WI, 2003.

[2] SADABS, Version 2.05, Bruker AXS Inc.; Madison, WI, 2002.

[3] G. M. Sheldrick, *Acta Crystallogr., Sect. A* **2008**, *64*, 112-122

[4] L. J. Barbour, *J. Supramol. Chem*. **2001**, *1*, 189-191.

[5] S. Takamizawa, E. Nakata, H. Yokoyama, *Inorg. Chem. Commun.* **2003**, *6*, 763-765.

[6] A. Kondo, H. Noguchi, S. Ohnishi, H. Kajiro, A. Tohdoh, Y. Hattori, W.-C. Xu, H. Tanaka, H. Kanoh, K. Kaneko, *Nano Lett.* **2006**, *6*, 2581-2584.

[7] K. Seki, *PCCP* **2002**, *4*, 1968-1971.

[8] P. K. Thallapally, B. Peter McGrail, S. J. Dalgarno, H. T. Schaef, J. Tian, J. L. Atwood, *Nat Mater* **2008**, *7*, 146-150